Journal of Alloys and Compounds xxx (xxxx) 175749

Contents lists available at ScienceDirect

Journal of Alloys and Compounds

journal homepage: www.elsevier.com/locate/jallcom

Predicting sensitivity to glucose in metal sulfides: A structural and surface characterization study

Julia M. Mazurków*, Anna Kusior, Andrzej Mikuła, Marta Radecka

Department of Inorganic Chemistry, Faculty of Materials Science and Ceramics, AGH University of Krakow, al. Adama Mickiewicza 30, Krakow 30-059, Poland

ARTICLE INFO

Keywords:
Transition metal alloys and compounds
Chemical synthesis
Catalysis
Electrochemical reactions
Electronic properties

ABSTRACT

The increasing prevalence of diabetes is leveraging the development of improved management technologies, including non-enzymatic glucose sensors that offer enhanced stability and longer operation times. However, the lack of reliable methods to predict materials' electrocatalytic activity remains a significant barrier to their advancement. Herein, we obtained transition metal sulfides (CuS, Ag_2S, FeS_2, and α-NiS) with similar shapes and sizes using wet chemical methods. Detailed structural and surface characterization revealed the presence of metals in mixed oxidation states and the formation of disulfides and polysulfides on the surface of air-exposed materials. The optical measurements supported by theoretical calculations indicated band gaps of 1.74, 0.98, and 1.14 eV in CuS, FeS_2, and Ag_2S, respectively. Nickel sulfide exhibited an intraband transition at 1.42 eV. The electrocatalytic activity toward glucose was investigated using cyclic voltammetry and chronamperometry. The lowest oxidation potential of 615 mV showed α-NiS, whereas the highest – Ag_2S (860 mV). The sensitivity determined in chronoamperometry measurements increased in the order of α-NiS > CuS > Ag_2S > FeS_2. Furthermore, selectivity studies revealed that FeS_2 responded only to strong reductants, while α-NiS to all examined electroactive species. In the last step, a clear relationship was identified between the d-band center position (d_{bc}) in metal sulfides and their electrochemical performance. The d_{bc} relative to the Fermi level is optimal in CuS and NiS (around −2 eV) for forming bonds with glucose and intermediates, while in Ag_2S and FeS_2, it lays too far or too close for effective electrooxidation.

1. Introduction

The search for new solutions to diabetes management is motivated by the constant growth of people suffering from this disease worldwide [1]. The dissemination of continuous glucose monitoring (CGM) systems has mitigated inconvenience for patients connected to frequent finger pricking. However, it also raised the requirements set for such systems involving longer operational time and higher chemical stability. Enzymes used in commercial sensors, such as glucose oxidase (GOx) and glucose dehydrogenase (GDH), tend to denature due to changes in temperature, pH, exposure to detergents, or prolonged interactions with electrochemically active substances present in the body fluids [2,3]. Additionally, the sensor lifetime can be limited by the enzyme leaching from the immobilization matrix or the dissociation of the non-covalently bonded cofactor [4]. These challenges have led to intensified efforts toward the development of non-enzymatic glucose sensors.

Transition metal sulfides (TMSs) have shown significant potential for electrochemical applications, including energy conversion and storage, as well as electrochemical sensors [5–8]. They are considered cost-effective alternatives to noble metals such as platinum and palladium. Owing to the lower electronegativity of sulfur, TMSs generally exhibit higher covalency in metal-anion bonding compared to their oxide counterparts, resulting in improved conductivity of these materials [6,9]. Additionally, sulfur's ability to catenate allows for the S-S bonds presence within metal sulfides. This feature is evident in disulfides, with FeS_2 being a prominent example. However, S-S bonds can also occur in monosulfides, e.g., covellite (CuS). This results in counterintuitive metal oxidation states in such compounds and the presence of sulfur active sites facilitating adsorption of reactant molecules. Furthermore, metal sulfides show diverse structures, including layered configurations characterized by anisotropic properties [9]. The structural flexibility also enables the formation of various defects (vacancies, interstitial atoms), leading to non-stoichiometric compositions. Those individual

* Corresponding author.
E-mail addresses: mazurkow@agh.edu.pl (J.M. Mazurków), akusior@agh.edu.pl (A. Kusior), amikula@agh.edu.pl (A. Mikuła), radecka@agh.edu.pl (M. Radecka).

https://doi.org/10.1016/j.jallcom.2024.175749
Received 14 May 2024; Received in revised form 12 July 2024; Accepted 28 July 2024

characteristics of TMSs offer the possibility to tune their electrochemical activity. However, an in-depth understanding of the fundamental properties of the most commonly studied metal sulfides is essential to fully leverage and optimize their electrochemical potential in various applications, including glucose sensors.

Copper, silver, iron, and nickel sulfides hold significant position as electrocatalysts [5,7]. Notably, CuS and α-NiS have been extensively studied for glucose electrooxidation, achieving high sensitivity and low detection limits [8,10,11]. However, they often encounter challenges with insufficient linear ranges, which are critical for accurate detection in blood or sweat. In contrast, Ag_2S and FeS_2 are predominantly employed in cathodic processes. Specifically, FeS_2 (pyrite) has been tested for the hydrogen evolution reaction (HER) [12], while Ag_2S has shown effectiveness in the electroreduction of CO_2 [5]. Despite the intensive works correlating various electronic structure-based descriptors with material electrocatalytic activity in water splitting processes [13,14], such an approach has not yet been applied to electrochemical sensors.

Two fundamental models are used to explain the electrocatalytic behavior of materials toward glucose. The chemisorption model proposed by Pletcher underlines the significance of the unpaired d-electrons and unfilled d-orbitals in bond formation between transition metal and adsorbate [15]. Additionally, it considers active site distribution on the surface (geometric requirement), especially when the molecule interaction with more than one site is expected, as in carbohydrates. This aspect explains why certain planes are more active than others. However, this model fails to account for the glucose electrooxidation by gold (with its filled d orbitals) in alkaline solutions. To address this issue, Burke introduced the Incipient Hydrous Oxide-Adatom Mediator (IHOAM) model, which identifies the critical role of the oxidation of the adatoms (surface atoms) to form an incipient hydrous oxide layer (OH_{ads}) at considerably lower potentials than those required for oxide monolayer growth [16]. These hydrous oxide species act then as electrocatalysts, offering a more accurate depiction of the behavior of metal- and metal oxide-based electrodes in alkaline conditions. Nevertheless, the IHOAM model does not comprehensively encompasses the effects of the transition metal's environment, such as in alloys, compounds (chalcogenides, nitrides, phosphides), or complexes.

This work integrates theoretical and experimental approaches to provide comprehensive insights into the structural and surface properties of metal sulfides (CuS, Ag_2S, FeS_2, and α-NiS). Our aim is to bridge the gap identified in the literature between these two standpoints. It is shown that various TMSs can be synthesized through wet chemical methods with consistent microspherical morphology to eliminate the influence of geometric factors. The bulk and surface compositions of the powders are thoroughly investigated to confirm phase purity. Furthermore, we comparatively study the electrochemical performance of TMS-modified glassy carbon electrodes. Density functional theory (DFT) calculations are used to complement the experimental findings on the materials' semiconducting properties and to provide electronic structure-related descriptors. A key novelty of this work is the identification of the d-band center position of the TMSs as an indicator of their sensitivity to glucose.

2. Experimental

2.1. Synthesis of metal sulfides

In order to obtain selected metal sulfides with similar ball-like morphology and desired phase composition, the synthesis strategies were adjusted for each material individually, as described in the Supporting Information (SI). Crucial parameters that influenced these features were determined. All samples and their synthesis conditions are summarized in Table S1.

2.2. Characterization of metal sulfides

The obtained materials were investigated using scanning electron microscope (SEM), transmission electron microscope (TEM), X-ray diffraction (XRD), Raman spectroscopy, X-ray photoelectron spectroscopy (XPS), X-ray absorption spectroscopy (XAS), dynamic light scattering method (DLS), Brunauer-Emmett-Teller method (BET), and diffuse reflectance spectroscopy (DRS). Details are provided in the SI.

2.3. Preparation of modified electrodes

The modified electrodes were prepared according to the procedure described elsewhere [17]. In 10 mL of aqueous solution with 0.1 g of dissolved PVP, 0.025 g of the appropriate metal sulfide was dispersed by mixing for 30 min and applying ultrasounds for 10 min. Then, 10 μL of as-prepared suspension was casted on the activated glassy carbon electrode (GCE) and left to dry overnight. The electrodes were stored in the refrigerator when not in use.

2.4. Electrochemical measurements

In order to evaluate the electrochemical performance of the modified electrodes, electrochemical impedance spectroscopy (EIS), cyclic voltammetry (CV), and chronoamperometry (CA) measurements were performed. Experimental details are given in the SI.

2.5. Computational details

All the considered materials were subjected to calculations based on the CuS ($P6_3/mmc$), Ag_2S ($P2_1/c$), FeS_2 ($Pa\bar{3}$), and α-NiS ($P6_3/mmc$) initial structures prepared by VESTA software [18]. Computational investigations were carried out utilizing the Wien2k package [19] employing the Full Potential Augmented Plane Waves (FP-LAPW) method within Density Functional Theory (DFT) and computational parameters as follows: PBEsol exchange-correlation potential [20], $Rk_{max} = 6.5$, $G_{max} = 14.0$. The energy and total charge differences of 10^{-5} Ry and 10^{-2} e were set as convergence criteria between individual SCF cycles. The structure relaxation was performed in full optimization procedure (unit cell parameters, atomic sites, and ionic relaxation) using Monkhorst-Pack k-points mesh proportional to the first Brillouin zone: 9x9x2, 8x4x4, 10x10x10, and 10x10x6 for CuS, Ag_2S, FeS_2, and α-NiS, respectively. Density of states (DOS) and band structures were generated on the basis of optimized structures using corrected modified Becke-Johnson (mBJ) potential [21] and denser k-points mesh (18x18x4, 16x8x8, 20x20x20, and 20x20x12 for CuS, Ag_2S, FeS_2, and α-NiS respectively). Additionally, the weighted averages of d-bands and p-bands were calculated and used for the estimation of the so-called electronic structure descriptors [14], namely d-band (d_{bc}) and p-band (p_{bc}) centers:

$$d_{bc} = \frac{\sum_{i=1}^{n} \left(d_{xy,i} + d_{xz,i} + d_{yz,i} + d_{x^2,i} + d_{x^2-y^2,i}\right) \cdot E_{eV,i}}{\sum_{i=1}^{n} \left(d_{xy,i} + d_{xz,i} + d_{yz,i} + d_{x^2,i} + d_{x^2-y^2,i}\right)} \quad (7)$$

$$p_{bc} = \frac{\sum_{i=1}^{n} \left(p_{x,i} + p_{y,i} + p_{z,i}\right) \cdot E_{eV,i}}{\sum_{i=1}^{n} \left(p_{x,i} + p_{y,i} + p_{z,i}\right)} \quad (8)$$

where $d_{xy,i} + d_{xz,i} + d_{yz,i} + d_{x^2,i} + d_{x^2-y^2,i}$ and $p_{x,i}$, $p_{y,i}$, $p_{z,i}$ correspond to the probability to find electrons in the respective d and p orbitals for Cu/Ag/Fe/Ni and S; $E_{eV,i}$– energy that corresponds to the probability of finding an electron at an individual orbital. A schematic illustration of

the relationship between conducted experiments and theoretical calculations is shown in Fig. S1.

3. Results and discussion

3.1. Morphological and structural characterization of metal sulfides

Synthesis of metal sulfides with diverse crystal structures (Fig. S2) while maintaining similar shape, size, and assumed phase composition presents significant challenges. To achieve this goal, we employed various wet chemical techniques, including synthesis at moderate temperatures (CuS), chemical conversion (Ag_2S), and hydrothermal method (FeS_2 and α-NiS). Based on the comprehensive literature review, the synthesis parameters were carefully optimized (Table S1). The structural characterization of the obtained materials involved XRD, SAED, and DRS (bulk methods), as well as Raman spectroscopy and XPS (surface-sensitive methods).

The synthesis procedure of spherical CuS was proposed based on our previous work [22]. In order to avoid precipitation of the intermediate phases, which would induce the tubular morphology of the final product, the mixing of copper sulfate with sodium thiosulfate was carried out in the aqueous solution preheated to 70 °C in a water bath. As can be seen in the SEM image (Fig. 1a), the obtained copper sulfide was in the form of spheres with an average hydrodynamic diameter of 1.3 ± 0.2 μm (Fig. S3) and a specific surface area of 2.2 m^2/g. Based on EDS analysis (Fig. S4), the ratio of Cu:S was determined to be 51:49 at%, closely aligning with the stoichiometric ratio. XRD measurements (Fig. S5) confirmed that the crystal structure of the synthesized material matched the characteristic peaks of the targeted hexagonal phase, covellite. Furthermore, Raman spectroscopy (Fig. S6a) indicated the presence of S-S bonds (strong band at 471 cm^{-1}), as expected from the arrangements of atoms in the unit cell of covellite (Fig. S2a).

Tuning the morphology of low-symmetry materials is hindered by the inherent asymmetry and complexity of the crystal structure. The different crystallographic planes in monoclinic structures may have varied growth rates, affecting the predictability and control of the final shape. By using a template-assisted strategy, it is possible to bypass this limitation. In our previous work, based on the example of tubular CuS, we have shown a facile method for its conversion to Ag_2S [23]. Following the same protocol, we successfully applied this technique to spherical CuS particles. SEM observations confirmed that the overall morphology was maintained (Fig. 1b), but the surface development was slightly decreased (0.5 m^2/g). The average hydrodynamic diameter remained similar, 1.4 ± 0.2 μm (Fig. S3). In the case of phase composition, the target monoclinic silver sulfide was obtained, albeit with metallic silver impurities, constituting 7 wt% as determined by Rietveld refinement. This observation is in agreement with the EDS results (Fig. S4b), which indicated an excess of silver in the sample (Ag:S ratio of 2.3:1.0 instead of a stoichiometric ratio of 2.0:1.0). Additionally, copper residues were detected at the level of ~2 at%. In the Raman spectra (Fig. S6b), a broad band between 140 and 260 cm^{-1} was observed, which could be assigned to Ag-S-Ag symmetric stretching modes [24,25].

Although pyrite is the most abundant sulfide mineral [26], its laboratory synthesis requires a careful selection of process parameters. Above pH 5, pyrite (cubic polymorph) is generally a more thermodynamically stable phase than marcasite (orthorhombic polymorph) [27]. Furthermore, longer reaction times and a higher Fe:S ratio were reported to facilitate pyrite formation. The suitable synthesis temperature window was established between 200 and 230 °C [12,28,29]. Based on these observations, we set the reaction time at 24 h and the Fe:S ratio at 1:8. Then, we investigated the influence of the synthesis temperature (180–205 °C), the sulfur precursor (thioacetamid, TAA or $Na_2S_2O_3$), and the pH-controlling reagent (hydrazine or ammonium buffer) on the phase composition and shape of the final product (Table S1). As can be seen in Fig. S7, temperature had little effect on the morphology but significantly affected the crystallinity and purity of the material. Only at 205 °C it was possible to eliminate the contribution of marcasite and, at the same time, enhance the crystallinity of the product. Replacement of TAA with sodium thiosulfate resulted in multiphase product formation and induced significant changes in the particles' shape (Fig. S7d). Additionally, the choice of the pH-controlling reagent proved essential for

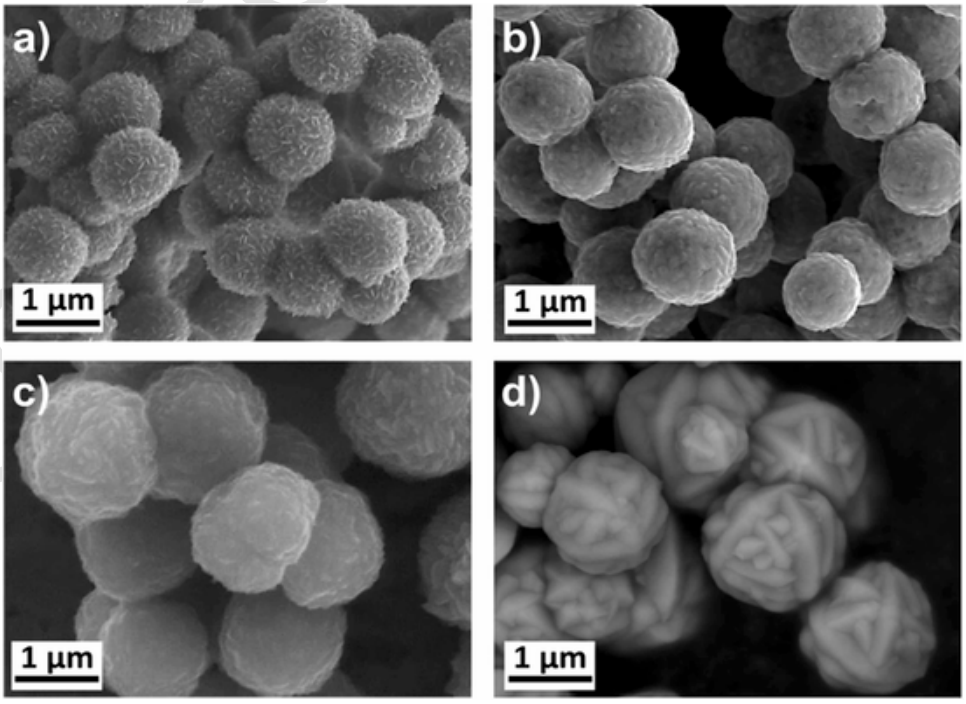

Fig. 1. SEM images of CuS (a), Ag_2S (b), FeS_2 (c), and α-NiS (d).

achieving spherical FeS_2 (Fig. S7c,e). For further experiments, the sample synthesized at 205 °C with hydrazine and TAA was chosen (Fig. 1c and Fig. S7c). The determined particle size for this material was 1.2 ± 04 μm, whereas the specific surface area was 6.4 m^2/g (Table 1). The EDS analysis indicated that the evaluated Fe:S ratio 33:67 at% perfectly matched the stoichiometric ratio (Fig. S4c). Raman spectroscopy further confirmed phase purity and the presence of disulfide ions (Fig. S2c). Only bands characteristic for S-S bonds in pyrite were observed in the spectrum at 338 (E_g mode), 374 (A_g mode), and 422 cm^{-1} (T_g mode) (Fig. S6c) [30].

In contrast to β-NiS (millerite, rhombohedral), the alpha polymorph of nickel sulfide (hexagonal) is a high-temperature phase [31]. Consequently, elevated synthesis temperatures tend to promote the formation of α-NiS. Within the hydrothermal synthesis approach, solvent selection also plays a crucial role, as it directly affects the pressure generated in the reaction vessel [32]. By setting the temperature to 200 °C, we investigated the influence of the water-EG ratio on the morphology and phase composition of the samples. As can be seen in Fig. S8, the presence of ethylene glycol (EG) facilitated the synthesis of the pure α-NiS phase (the recorded pressure in the H_2O:EG = 0:1 solution was 5 bar), whereas the multiphase product was obtained from water (the recorded pressure in the H_2O:EG = 1:0 solution was 1 bar). From a morphological perspective, the targeted spherical shape of the particles was achieved using the H_2O:EG = 1:1 solution (Fig. 1d and Fig. S8c). Additionally, the slight excess of sulfur (n_{Ni}:n_S = 3:4) was beneficial for eliminating β-NiS and simultaneously preventing the formation of NiS_2. This conclusion aligns well with the phase diagram for the Ni-S system [31]. Therefore, the sample synthesized from the H_2O:EG = 1:1 solvent with a n_{Ni}:n_S ratio of 3:4 was chosen for further studies. The Ni to S ratio determined by the EDS analysis (51:49) agreed well with the stoichiometric one (Fig. S4d). As expected (Fig. S2d), no distinct bands related to S-S bonds were detected on the Raman spectra (Fig. S6d).

Table 1
Summary of parameters determined from XRD, DLS measurements, BET analysis, and DRS.

Method	Parameter	CuS	Ag_2S	FeS_2	α-NiS
XRD	Crystallite size (nm)	144	589	594	379
DLS	Hydrodynamic diameter (μm)	1.3 ± 0.2	1.4 ± 0.2	1.2 ± 0.4	1.3 ± 0.2
BET	Specific surface area (m^2/g)	2.2	0.5	6.4	6.8
DRS	Optical band gap, E_g (eV) / type	1.74 / direct	0.98 / direct	1.14 / indirect	1.42 / direct

3.2. TEM analysis

The morphology and structure of the obtained metal sulfides were further studied using TEM. Elemental mapping for all samples confirmed the uniform distribution of both metal and sulfur within the particles (Fig. 2a-d). For Ag_2S, an additional copper contribution was detected, though it remained below the quantification limit. Furthermore,

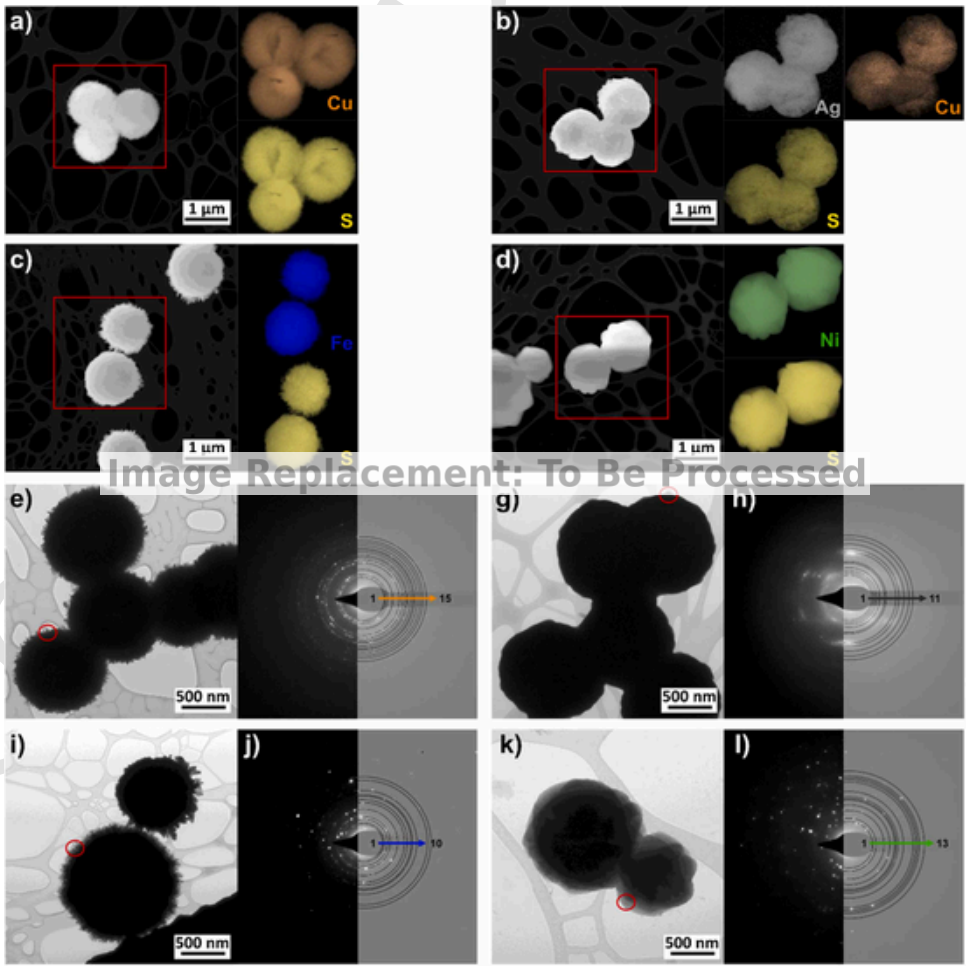

Fig. 2. Dark-field TEM images with EDS mapping of the regions marked by the red frame (a-d), bright-field TEM images (e,g,i,k), and SAED patterns with numbered rings of the regions marked by the red circles (f,h,j,l) for: CuS (a,e,f), Ag_2S (b,g,h), FeS_2 (c,i,j), and α-NiS (d,k,l).

the selected area diffraction (SAED) analysis of the samples (Fig. 2e-l) proved the dominant presence of targeted phases, namely covellite, acanthite, pyrite, and α-NiS, within the CuS, Ag_2S, FeS_2, and NiS samples, respectively. Interestingly, no signal from metallic silver in Ag_2S was observed. Although XRD analysis and Raman spectroscopy indicated that pure pyrite was achieved in the FeS_2 sample, an additional d-spacing of 3.442 Å was visible on the SAED pattern, characteristic of the marcasite (110) plane. In the study by Yuan et al., it was shown that at the beginning of the hydrothermal reaction, marcasite and pyrite crystalize simultaneously [29]. Subsequently, marcasite slowly transforms into pyrite at increased temperatures, accounting for the residual contribution of this phase in the FeS_2 sample. Moon et al. reported that marcasite preferentially remains at the particles' boundaries [33], which may explain why its presence was detected using SAED and not other techniques (see the red circle indicating the region from which the signal was collected in Fig. 2i). A comprehensive list of detected d-spacings, along with the corresponding compounds and planes for all samples, is provided in Table S2.

3.3. XPS analysis

The surface composition of metal sulfides may differ significantly from the bulk due to the tendency of sulfur to form dimers and polysulfides (catenation). This behavior, in turn, may lead to changes in the oxidation states of metals on the surface and affect the electrochemical performance of these compounds [9,34–36]. Therefore, XPS analysis was conducted to elucidate the surface composition of all metal sulfides. Table S3 lists the peak positions, the assigned specific groups, and their surface contributions.

Copper sulfide has a specific structure with CuS_4-CuS_3-CuS_4 layers separated by S-S bridges (see Fig. S2a), which accounts for the counter-intuitive oxidation states of copper and sulfur in this compound. A closer insight into the Cu $2p_{3/2}$ spectrum presented in Fig. 3a revealed that the main line was positioned at 932.9 eV, indicating the presence of copper in the first oxidation state rather than in the second. The asymmetric tail visible on the higher energy side of the peak can be a result of 1) kinetic energy losses typical for metals [37,38] or 2) the presence of Cu(II) at the surface. The lack of shake-up lines between the 940–947 eV characteristic for Cu^{2+} seems to support the first option. To clarify this issue, XAS measurements were performed in two modes – surface-sensitive TEY and depth PFY (Fig. S9). The Cu L_{23} edge spectrum for CuS resembles well that of Cu_2O. The small peaks at around 931 eV characteristic for Cu^{2+} disappeared when the signal was collected from deeper within the material. This observation may indicate that Cu(II) is specifically present at the surface of the air-exposed material. However, it does not negate the higher valences of copper than Cu^{1+} in the bulk unoxidized material, as proposed by other authors in the ionic models for covellite, namely $(Cu_2^{3+})(Cu^{1+})(S_2^{2-})(S^{2-})$ [39–41] or $(Cu^{1.33+})_3(S_2^{2-})(S^{2-})$ [38,42,43]. The oxidation state of copper is strongly correlated with the presence of both sulfide and disulfide

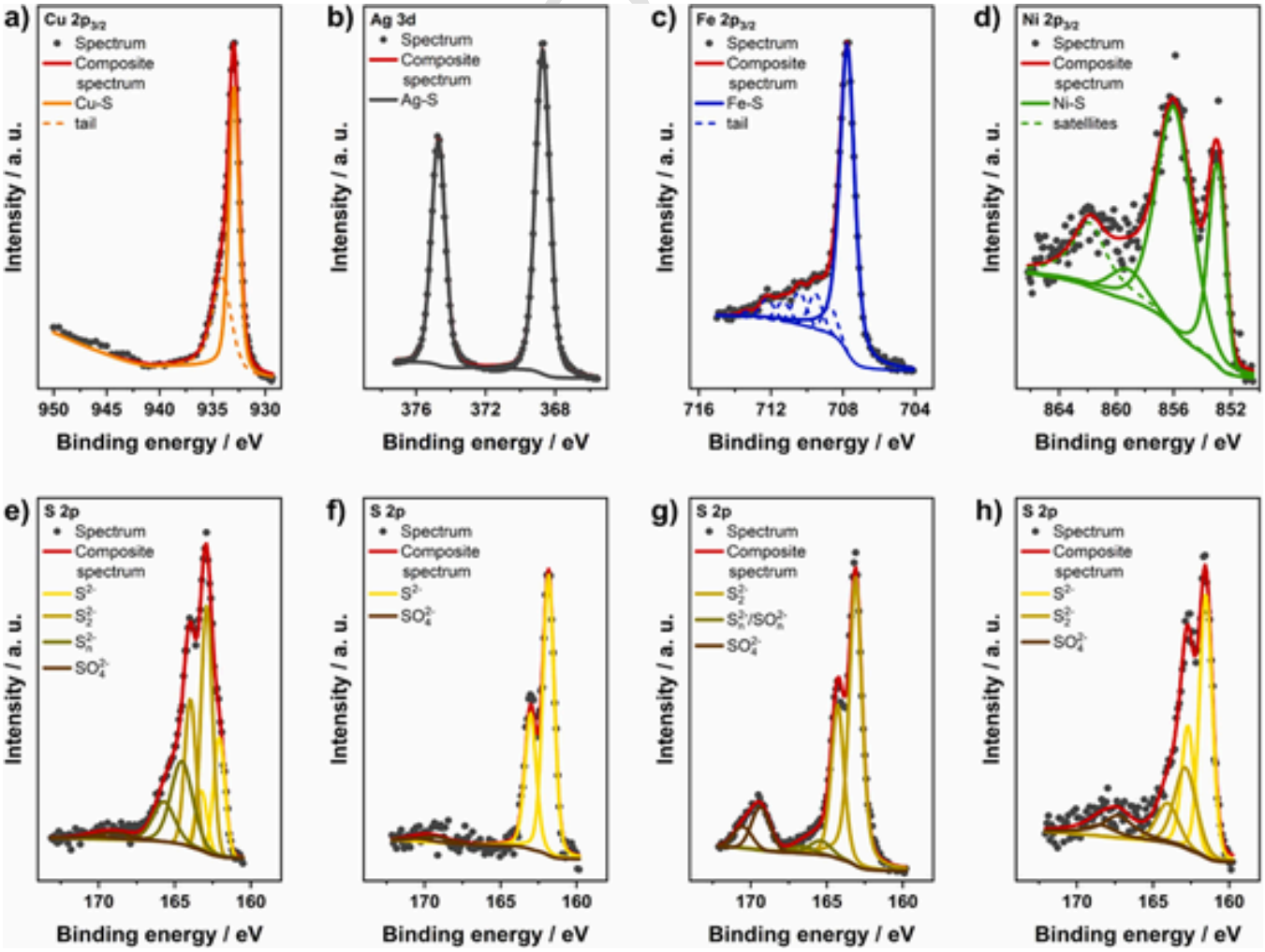

Fig. 3. High-resolution XPS spectra for: CuS (a,e), Ag_2S (b,f), FeS_2 (c,g), and α-NiS (d,h).

bonds, as evidenced by the two doublets at 162.0/163.2 and 162.8/164.0 eV visible on the S 2p spectrum (Fig. 3e). The calculated area ratio of these peaks was 1:2.1, close to that expected for covellite (1:2). The additional doublets at 164.1/165.3 and 169.0/170.2 eV can be attributed to polysulfides and sulfates, respectively, forming on the air-exposed surface of metal sulfides [34,36].

In the Ag 3d spectrum for Ag_2S, only two well-defined symmetrical peaks were present at 368.7 and 374.7 eV (Fig. 3b), which can be assigned to the $d_{5/2} - d_{3/2}$ doublet characteristic for Ag^+. The slight shift toward higher energies compared the values reported in the literature may be explained by the contribution of metallic silver, as evidenced by XRD analysis [44,45]. This conclusion is also supported by an increased Ag:S ratio of 2.5:1 in the sample instead of a stoichiometric ratio of 2:1 (Table S3). The origins of the metallic silver in the sample were discussed in our previous work [23]. The S 2p spectrum was fitted with two doublets positioned at 161.8/163.0 and 169.4/170.6 eV (minor) arising from sulfide and sulfate ions, respectively. Additionally, to elucidate the chemical state of copper detected by EDS, the Cu $2p_{3/2}$ line was analyzed (Fig. S10). The positions of the recorded lines indicated the presence of copper (Cu^{2+}) bonded in oxides and sulfates, as confirmed by the satellites, while no characteristic peaks for copper sulfide were observed. It suggested that the conversion from CuS to Ag_2S was complete, though some copper impurities remained. Silver, as a soft acid and semi-precious metal, exhibits lower reactivity than other transition metals in this work. Therefore, its surface composition is similar to the bulk material (Fig. S2b). Only in the case of silver compounds the standard formation enthalpy of sulfide is lower (more negative) than for oxide.

The Fe 2p3/2 spectrum of FeS_2 (Fig. 3c) is characterized by a dominant peak at 707.8 eV, indicative of bulk Fe^{2+} in pyrite [46,47]. The interpretation of the following low-intensity tail remains more ambiguous as its shape diverges from satellite and shake-up peaks or the typical Fe metal tail. Nesbitt et al. proposed that it arises from multiplet contributions of surface Fe(II)-S, Fe(III)-S, and Fe(III)-O bonds [48]. Such surface species inherently possess unpaired electrons in the 3d valence band. The S 2p region for this sample was fitted by three doublets ($2p_{3/2}/2p_{1/2}$) at 163.0/164.2, 165.4/166.6, and 169.3/170.5 eV (Fig. 3g). The first doublet was ascribed to disulfide ions of pyrite (Fig. S2c), whereas the last one to sulfates [47,48]. The second minor doublet could be assigned to polysulfides and/or oxidized species of sulfur reported by Nesbitt et al. on air-oxidized pyrite surfaces [48]. The expected contribution from monosulfide ions was not observed.

As shown in Fig. 3d, the Ni $2p_{3/2}$ region for α-NiS is composed of three peaks at 853.0, 856.0, and 861.9 eV, which can be ascribed to Ni^{2+}, Ni^{3+}, and a satellite, respectively. The presence of nickel in the third oxidation state in α-NiS was also observed by other authors [49–51]. It may be explained by an excess of sulfur at the surface, as evidenced by the determined composition summarized in Table S3. The S 2p spectrum was deconvoluted into three doublets, $2p_{3/2}/2p_{1/2}$ (Fig. 3h). The component at 161.5/162.7 eV was attributed to disulfide ions, whereas the second one at 162.9/164.1 eV to disulfide ions present on the surface. The low-intensity doublet at higher energies arises from partial oxidation of sulfur due to exposure to air. These results indicated a significant difference between the surface and the bulk of α-NiS (Fig. S2d). The occurrence of nickel at two valence states is expected to promote redox reactions, thereby boosting the electrochemical activity of nickel sulfide [49,51].

3.4. DRS analysis

To experimentally assess the semiconducting properties of selected metal sulfides, DRS measurements were conducted. The obtained copper sulfide was characterized by a direct optical band gap (E_g) of 1.74 eV (Fig. 4a,b), slightly below the most commonly reported value of around 2.00 eV but within the encountered range of 1.60–2.20 eV [52]. This variation may stem from the bulk properties of our sample, in contrast to the nanoscale materials preferentially studied in the literature, which exhibit a blue shift of the band gap. The CuS sample had a dark teal color (Fig. 4i). The estimated direct E_g for Ag_2S was 0.98 eV (Fig. 4c,d) and fell perfectly within the expected range of 0.90–1.10 eV for bulk material [7]. This powder was dark gray (Fig. 4j). As suggested by Ferrer et al., the analysis of the UV-ViS spectrum for FeS_2 (Fig. 4e) was performed using the Kramer-Krönig method [53]. Initially, to obtain the absorption spectrum, the real and imaginary parts of the reflectance spectrum were calculated [54]. Subsequently, based on the Tauc plot $(\alpha h\nu)^{1/2}$ versus $h\nu$ (Fig. 4f), the indirect band gap of 1.14 eV was determined. This E_g was comparable to the most commonly cited value of 1.00 ± 0.11 eV [12,29,53]. Interestingly, the recorded edge was weak, with a change in the reflectance of around 1 %. It may be due to (1) the presence of marcasite (Fig. 2j), which has a narrow band gap of around 0.34 eV [47], as well as (2) the defects on the pyrite surface (as evidenced by XPS, Fig. 3c,d) causing the emergence of new states within the band gap and therefore modifying the spectrum [55]. In the case of α-NiS, the Kubelka-Munk function revealed a direct band gap of 1.42 eV. There is no agreement in published studies on the optical band gap of this material. Some works give the value of around 0.45 eV [56], whereas others claim that nickel sulfide is a wide-band gap semiconductor [57]. The crucial point is that edges visible on the diffuse reflectance spectra do not always originate from the fundamental band gap. The optical band gap is specifically related to the energy required

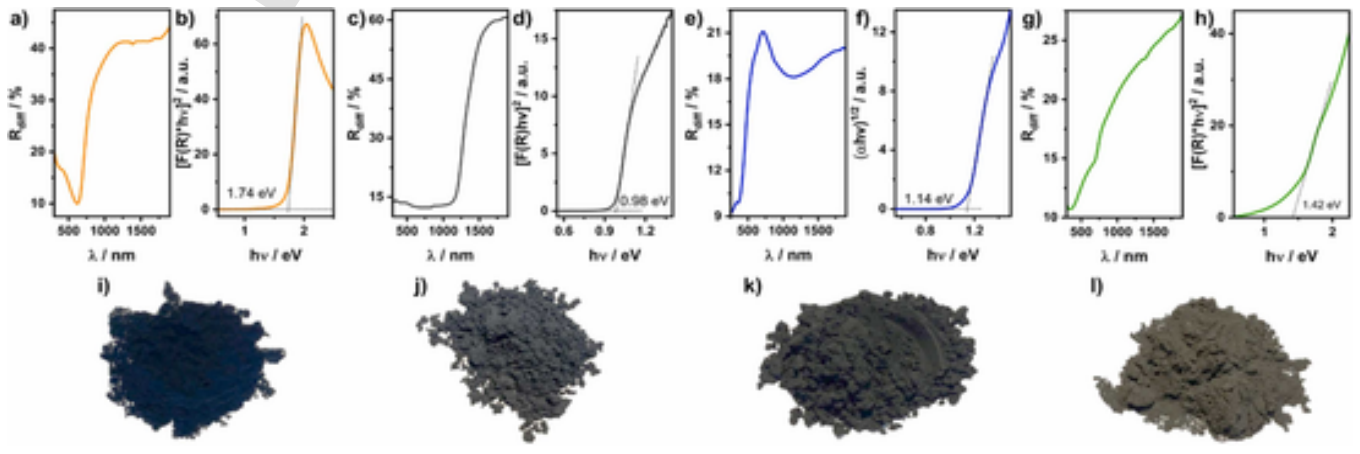

Fig. 4. UV-ViS diffuse reflectance spectra (a,c,e,g), Tauc plots (b,d,f,h), and images of the powders (i-l) for: CuS (a,b,i), Ag_2S (c,d,j), FeS_2 (e,f,k), and α-NiS (g,h,l).

for an electron to transition from the valence band to the conduction band upon absorbing a photon. Therefore, intraband transitions in the material may also be observed on the DRS spectrum.

3.5. Electrochemical measurements

To evaluate the general electrochemical activity of selected metal sulfides, firstly, EIS measurements were conducted in the electrolyte containing the redox couple $[Fe(CN)_6]^{3-/4-}$. Impedance spectra in Bode and Nyquist configurations are presented in Fig. 5. The obtained data were fitted with the equivalent circuit consisting of connected in series (1) an electrolyte resistance (R_e), (2) a parallel combination of constant phase element (CPE) and resistor (R) representing the charge transfer between GCE and modifier, as well as (3) a second parallel combination of CPE_{CT} and connected in series resistance (R_{CT}) and Warburg element (W_{CT}) illustrating the charge transfer between the solution and the modifier (inset of Fig. 5b) [17]. The determined equivalent circuit parameters (Table 2) showed that the GCE resistance dropped significantly after modification with metal sulfides, indicating improved charge transfer. The lowest R_{CT} (11.8 kΩ) and the highest heterogenic rate constant ($k = 4.93 \cdot 10^{-5}$ m/s) were obtained for GCE/CuS, whereas the poorest performance exhibited GCE/Ag_2S with the R_{CT} of 62.4 kΩ and k of $1.02 \cdot 10^{-5}$ m/s. The similar charge transfer resistance and Warburg impedance modulus of GCE/FeS_2 and GCE/α-NiS resulted in comparable k values for those electrodes. The relatively high differential capacity of the double layer (CPE_{CT}) for GCE/FeS_2 suggested that for this electrode, a high signal-to-noise ratio should be expected, increasing the background current in the voltammetry measurements. Electrochemically active surface areas (A) calculated from EIS measurements were used to achieve the current densities for each electrode.

The electrochemical performance of modified electrodes toward glucose was investigated by cyclic voltammetry (CV) and chronoamperometry (CA) measurements. The background curves recorded in 0.1 M NaOH (dashed lines in Fig. 6) for GCE/CuS and GCE/FeS_2 exhibited no pronounced peaks originating from the intrinsic material redox reactions. Only the onsets of oxygen evolution reaction (OER) were visible for those electrodes, which, in the case of GCE/FeS_2, considerably overlapped the glucose peak at 725 mV (visible only after applying background correction). For GCE/CuS, a distinct glucose oxidation peak (E_{ox}) formed at 650 mV and continued on the cathodic scan until the surface was inactivated upon reaching the reduction potential [10]. Fleischmann et al. proposed that the Cu(II)/Cu(III) transition occurs around 685 mV (vs. Ag/AgCl) on bare copper electrodes in alkaline electrolytes, but it is screened by the oxygen evolution signal [58]. On the other hand, the GCE/Ag_2S background behavior was very complex (Fig. 6b). Although XRD analysis identified traces of Ag within the converted Ag_2S, our previous research indicated that silver sulfide's voltammogram in NaOH resembles metallic silver, regardless of the impurities [23]. The first two peaks on the anodic scan (A_1, A_2) can be ascribed to the formation of Ag(I) compounds, followed by their oxidation to Ag(II) and Ag(III) species (peaks A_3 and A_4, respectively). Upon glucose addition, only the A_4 and A_5 peaks increased, whereas the others decreased. This observation contrasts with the findings of the study by Luo et al. on silver electrodes, in which an additional peak was emerging at around 200 mV [59]. Our experiments did not reveal this peak, suggesting that glucose oxidation was mediated by high-valent surface oxides. The CV curve of GCE/α-NiS was characterized by two well-defined peaks at 560 (anodic scan, A_1) and 400 mV (cathodic scan, C_1) corresponding to the Ni(II)/Ni(III) redox couple, similar to metallic nickel [59]. The signal from glucose coincided with A_1 but was slightly more positive (Fig. 6d). In the literature, it was postulated that forming at the material surface NiSOH species catalyze oxidation [60]. Considering the presented results, it is evident that E_{ox} is influenced by the transition metal in the compound and the potential at which the hydrous oxide layer forms, according to the IHOAM model [16]. Nonetheless, glucose oxidation potential can be tuned to some extent by the metal structural surrounding (i.e., the presence of sulfide or disulfide ions).

The as-determined E_{ox} was applied for the CA detection of glucose (Fig. 7a). Sensitivity (S), limit of detection (LOD), and limit of quantification (LOQ) were calculated based on the calibration curves. Interestingly, the amperometric response from GCE/FeS_2 was too weak to distinguish from the background current. Even after reducing the potential to 600 mV, subsequent glucose additions did not yield a discernible signal. The highest sensitivity was noted for GCE/α-NiS. The dual valency of nickel sulfide (Fig. 3d) facilitated the weakening of the metal-adsorbate bonds, enhancing its electrochemical performance [15]. However, the electrode response disproportionately increased with each subsequent addition of the same glucose concentration, resulting in elevated LOD and LOQ values of 0.11 mM and 0.35 mM, respectively. This observation may be attributed to new active site formation on the nickel sulfide when subjected to a constant potential difference. The GCE/CuS electrode exhibited slightly decreased sensitivity but significantly improved LOD and LOQ, 0.04 and 0.13 mM, respectively. For GCE/Ag_2S, the lowest sensitivity was obtained, while the LOD and LOQ remained similar, 0.02 and 0.05 mM, respectively. The parameters of the modified electrodes are summarized in Table S4. Selectivity studies (Fig. 7b) revealed that GCE/FeS_2 responded only to moderate and strong reductants, such as acetaminophen (AP), uric acid (UA), and ascorbic acid (AA). On the other hand, despite the lowest applied po-

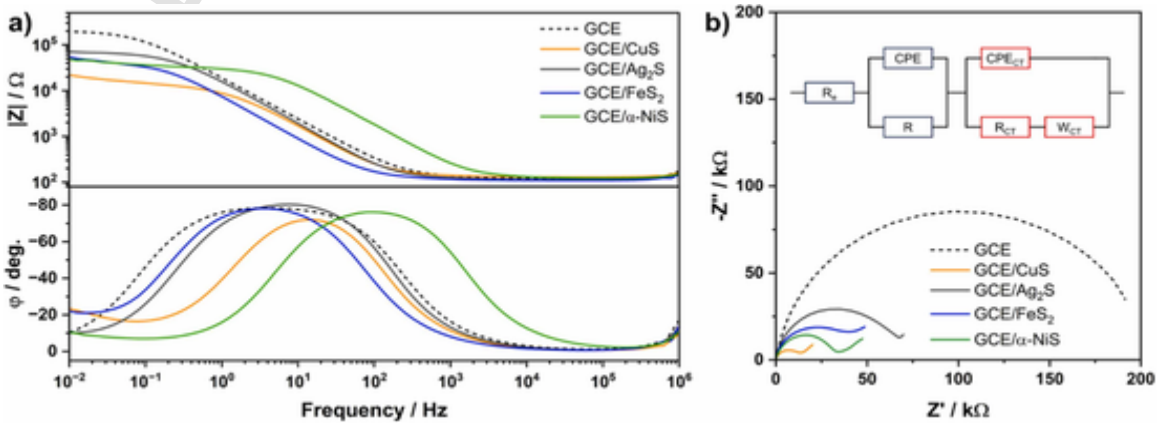

Fig. 5. Impedance spectra in Bode (a) and Nyquist configurations (b) measured in the electrolyte containing 0.1 M KCl + 1 mM $[Fe(CN)_6]^{3-/4-}$ for bare GCE, GCE/CuS, GCE/Ag_2S, GCE/FeS_2, and GCE/α-NiS. The inset shows the equivalent circuit.

Table 2
Summary of the equivalent circuit parameters, heterogenic rate constants (k) and electrochemically active surface areas (A) for bare GCE and modified electrodes.

Electrode	R_{CT} (kΩ)	W_{CT} (kΩ/s$^{1/2}$)	CPE_{CT} (μF)	k × 10^{-5} (m/s)	A (mm^2)
GCE	198.0	1.65	9.7	0.17	8.37
GCE/CuS	11.8	3.07	12.4	4.93	4.50
GCE/Ag_2S	62.4	3.34	10.7	1.02	4.13
GCE/FeS_2	36.2	5.52	22.5	2.90	2.50
GCE/α-NiS	31.6	4.25	1.5	2.54	3.24

tential, GCE/α-NiS gave the signal to all the investigated electrochemically active species. This conclusion aligns well with previously published works on the selectivity of nickel-based glucose sensors [60]. GCE/CuS and GCE/Ag_2S electrodes were inactive to urea (weak reductant). Although the IHOAM model can generally explain the potentials required for glucose oxidation, it fails to offer a foundation for predicting sensitivity to glucose.

3.6. DFT calculations and theoretical analysis

To find a descriptor enabling to predict the sensitivity of the selected TMSs toward glucose, obtained electrochemical data were interpreted in the context of theoretical calculations. Additionally, the results from the DSR measurements were revisited based on the band structure of the materials. Determined parameters, such as fundamental band gap, bond lengths, and d-band centers, are summarized in Table 3.

The band structure (Fig. S11a) and density of states (Fig. 8a) for copper sulfide characterized by a covellite structure reveal a direct band gap of 0.40 eV. Similar results were obtained in the study by Morales-Garcia et al., where the generalized gradient approximation functional supplemented with a localization correction provided by the Hubbard model (GGA + U, with U = 5 eV) method was utilized [41]. However, the local-density approximation (LDA) + U approach adopted by Deng et al. allowed for predicting the higher band separation of 1.76 eV [61], which correlates with the value obtained in our DRS measurements (Fig. 4a,b). The shape of the band curves and the partial density of states (DOS) near the Fermi level indicate a significant contribution of the occupied states. Particularly interesting in this regard seems to be the interplay between the covellite structure (Fig. S2a) and its electronic structure properties. The sulfur atoms coordinating the CuS_4

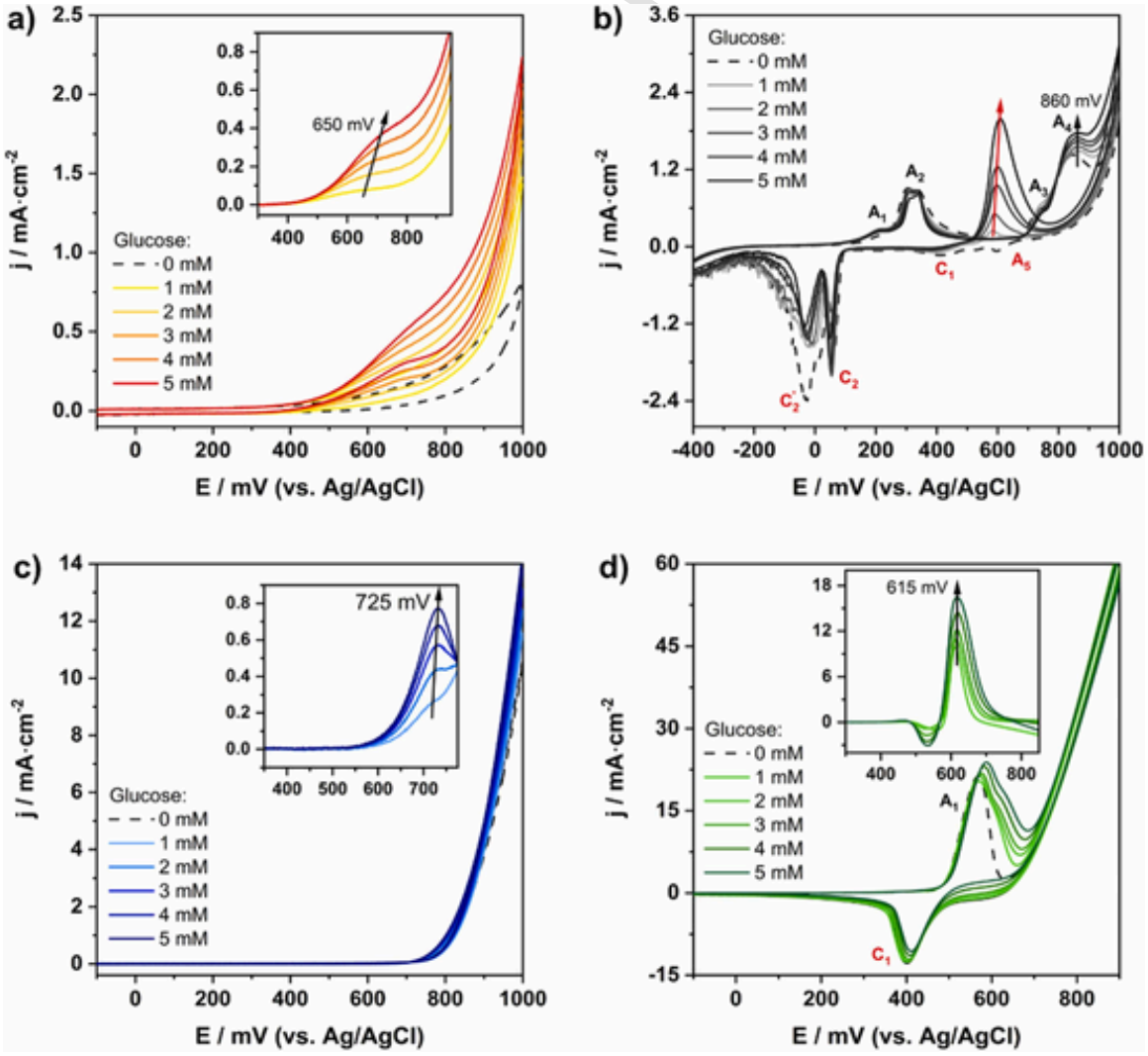

Fig. 6. Cyclic voltammograms recorded upon subsequent addition of glucose (concentration range: 0–5 mM, scan rate: 100 mV/s) with insets showing anodic curves after background subtraction for: GCE/CuS (a), GCE/Ag_2S (b), GCE/FeS_2 (c), and GCE/α-NiS (d).

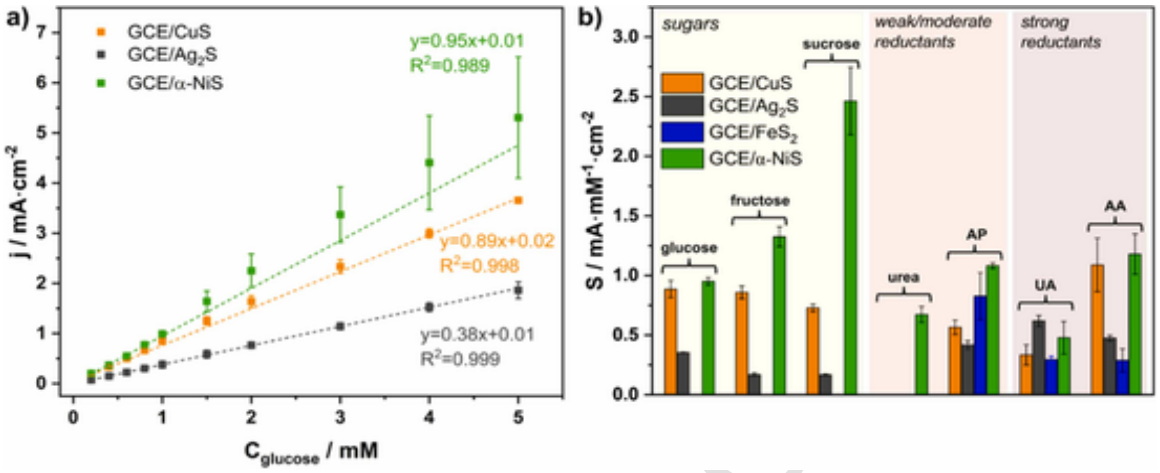

Fig. 7. Calibration curves (a) and sensitivity values for selected electrochemically active species (b) determined in chronoamperometry measurements under the glucose oxidation potential for GCE/CuS, GCE/Ag_2S, GCE/FeS_2, and GCE/α-NiS.

Table 3
Summary of parameters determined from theoretical calculations.

Parameter	CuS	Ag_2S	FeS_2	α-NiS
Fundamental band gap (eV) / type	0.40 direct	1.01 direct	0.90 indirect	no
Semiconductor type	p	n	p	-
S-S bond length (Å)	2.117	-	2.196	-
M-S bond length (Å)	2.272(3x)/2.322 (1x) (tetrahedral) 2.167 (trigonal)	2.485/2.499/2.611 (trigonal) 2.437/2.440 (planar)	2.225	2.347
M d-band center, d_{bc} (eV)	−2.23	−3.85	−0.42	−2.10
S p-band center, p_{bc} (eV)	−1.84	−1.63	−1.67	−3.32

tetrahedra that simultaneously form S-S bonds between the layers (2.117 Å) possess their highest occupied states, which are only partially filled, located at higher energies in comparison to the sulfur atoms coordinating the triangular plane CuS_3 (Fig. S2a). It implies that the Fermi level area is mainly surrounded by occupied S 3p states with a much smaller contribution of Cu 3d states, indicating that the Cu-S bonds in CuS_4 are weaker than the interlayer S-S bonds. DOS also shows that the states with the highest contribution near the Fermi level are Cu d_{xy} and $d_{x^2-y^2}$, as well as the S p_x and p_y states. Both of the aforementioned effects point to a strong anisotropy in the electrical and electrochemical properties of CuS [41]. Additionally, the calculated electronic structure descriptors reveal that the d_{bc} and p_{bc} are located relatively deep in the valence band. It suggests that CuS should exhibit higher activity toward electrochemical processes occurring on anodes.

The electronic structure (Figs. 10b and 8b) of low-temperature Ag_2S characterized by monoclinic structure (Fig. S2b) indicates an n-type semiconductor behavior, with a band gap of approximately 1.01 eV. This result agrees well with the optical band gap of 0.98 eV estimated from DRS measurements (Fig. 4c,d). The valence band of this material is primarily composed of Ag 4d and S 3p states. In the lower energy region, there is a significant overlap between the hybridized Ag 5 s and S 3p states that form bonding bands. In the higher energy region, Ag 4d and S 3p form antibonding bands, and finally, nonbonding and unoccupied states near the Fermi level. The bottom of the conductance band, in turn, is composed mainly of sulfur 3p states with a minor contribution of Ag 4d states. From the electrocatalytic standpoint, silver(I) sulfide exhibits a d-band center located very deep with the valence states, which stem from silver coordination and hybridized states at the lower energy region of the valence band. This observation implies that the material should exhibit likely activity for anodic processes but considerably low general electrochemical activity.

Generally, the band structure (Fig. S11c) and DOS (Fig. 8c) indicate that FeS_2 should be considered a p-type semiconductor with an indirect band gap of approximately 0.90 eV. This estimation aligns with other theoretical predictions [62], though it is slightly lower than the experimentally determined value of 1.14 eV (Fig. 4e,f). It may be attributed to the relatively flat valence and conduction bands, whereas the Tauc plot method better reflects transitions within parabolic band edges [53]. In the energy range of approximately −6.0–1.2 eV, several bands originating from a fusion of the Fe 3d and S 3p orbitals can be observed. Closer to the Fermi level and below the valence band maximum, another group of bands arises, mainly from the 3d iron states. The conduction band, in turn, consists of the states emerging from the unoccupied Fe 3d shell and, to a lesser extent, from the S 3p states, with their relative contributions gradually shifting as the energy level rises. The transition from Fe 3d to S 3p character can be observed, especially in the lowest conduction band region, where at Γ point, the band is solely attributed to the S 3p states, but due to hybridization with the Fe 3d states, it loses this domination toward the X and R points (Fig. S11c). From the point of view of determined electronic structure, the additional peaks observed on the UV-ViS spectrum at 1.74 and 3.90 eV (Fig. 4e) can be assigned to the intraband transitions from Fe 3d and S 2p states, respectively, into the antibonding states [53,63]. In our model, the d_{bc} lies relatively close to the Fermi level, pointing to the potential activity toward cathodic processes, e.g., hydrogen evolution reaction (HER) [64].

The band structure (Fig. S11d) and DOS of α-NiS (Fig. 8d) indicate a material with a strongly metallic character, exhibiting no energy band gap. DOS between −4.0 and 1.3 eV is dominated by the Ni 3d states with a minor contribution from the S 3p states. Near the Fermi level, the extent of sulfur-based states increases owing to significant covalency in this system, forming antibonding states. The Fermi level lies close to the local minimum of DOS dominated by these states, creating the possibility of opening the band gap due to the instability of the Fermi surface (e.g., resulting from doping the anionic sublattice or phase transition) [65], what can explain the narrow band gaps reported in the literature [56]. The transition visible on our UV-ViS spectrum at 1.42 eV (Fig. 4g,h), as well as wide band gaps reported by other groups (i.e., 3.62 eV) [57] may be attributed to other transitions possible in the α-NiS as depicted in Fig. S12. Similarly to CuS, the d_{bc} lies considerably deep in the

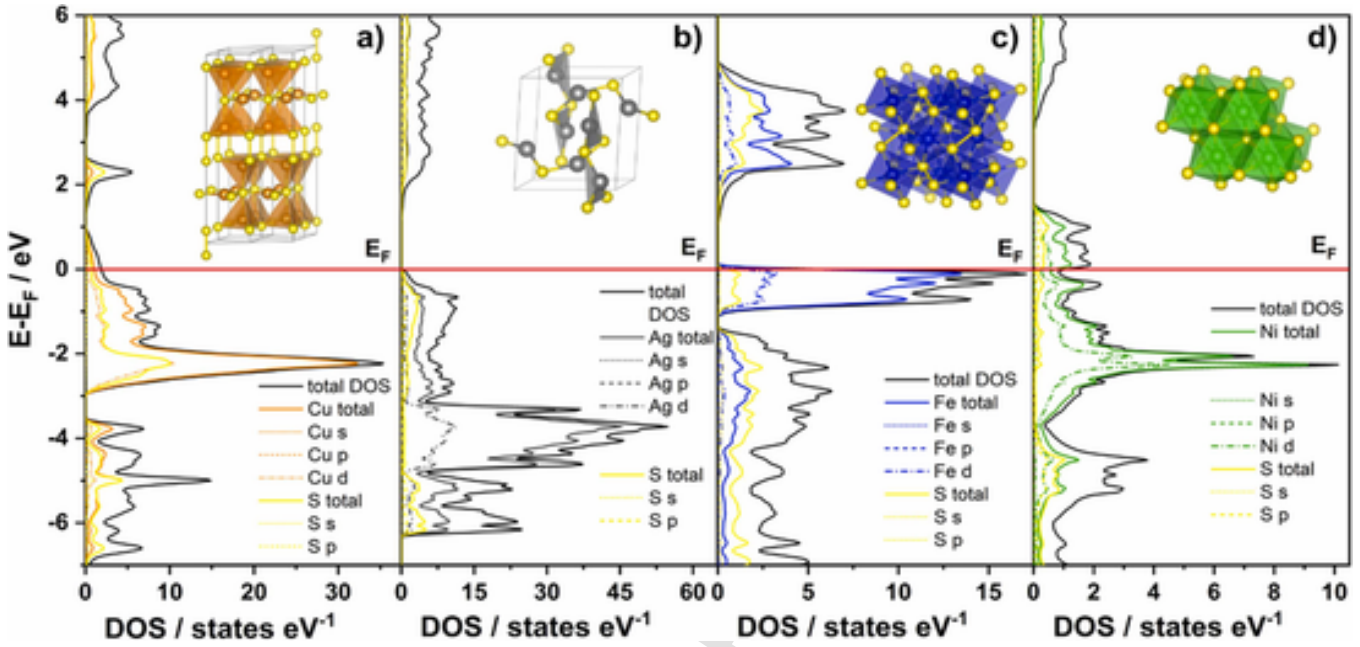

Fig. 8. Total and partial density of states with insets showing unit cells for CuS (a), Ag_2S (b), FeS_2 (c), and α-NiS (d).

valence level, suggesting that the hexagonal NiS should also exhibit the electrocatalytic potential toward anodic reactions.

In the field of non-enzymatic glucose sensors, the chemisorption and IHOAM models are the primary frameworks used to describe the electrochemical behavior of materials [10]. However, as discussed above, neither of these theories applies to all kinds of materials, especially beyond pure metals and their oxides. Thus, we sought a solution outside these conventional theories. For instance, Yamaguchi et al. developed statistical method to distinguish the critical properties influencing activity in CO_2 electroreduction [5]. It was shown that structural parameters (e.g., metal-sulfur bond length) affect carbon monoxide (CO) production, while electronic parameters (e.g., absolute electronegativity) determine formate ($HCOO^-$) production efficiency. Nonetheless, in the case of different electrocatalytic reactions (such as HER and OER), other descriptors were identified as relevant through pattern recognition methods [13,66], indicating the limited universality of this approach. The values of the most commonly considered parameters evaluated for our TMSs are summarized in Table S5. On the other hand, the d-band theory has proven its effectiveness in many fields, including energy conversion [67] and photocatalysis [68]. Therefore, we closely examined the relationship between the sensitivities toward glucose of selected metal sulfides and their estimated d-band center positions. As can be seen in Fig. 9, a clear correlation was obtained. Notably, for nickel and copper sulfides, d_{bc} positions around −2 eV vs. E_f resulted in comparably high electrocatalytic performance. Conversely, the shift of the d-band center toward lower values, as noted with Ag_2S, led to bonds weakening between the adsorbate and the material, thus hindering the catalytic reaction according to the Sabatier principle [69]. The negligible response in FeS_2 may be attributed to the formation of too strong bonds with glucose and/or the intermediate products. These findings are promising for predicting materials' sensitivity toward glucose, suggesting a potential pathway for advancing non-enzymatic glucose sensors.

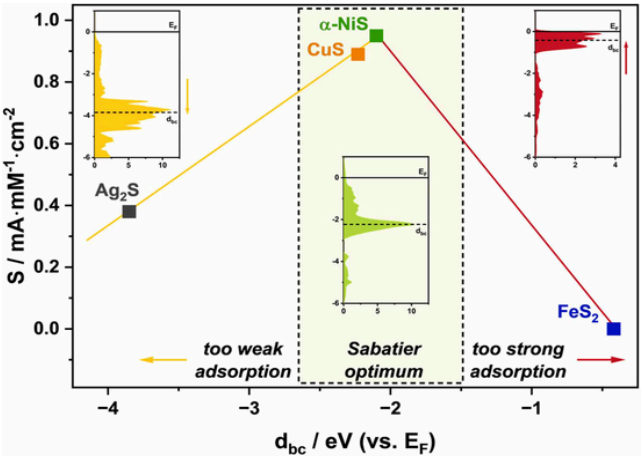

Fig. 9. Dependence of sensitivity toward glucose on the position of the d-band center in the metal sulfide.

4. Conclusions

In summary, selected metal sulfides (CuS, Ag_2S, FeS_2, and α-NiS) were successfully synthesized with a similar spherical shapes and micrometric sizes using wet chemical approaches. Extended structural characterization revealed the phase purity of copper sulfide (covellite) and nickel sulfide (α-NiS). The chemical conversion of CuS enabled to receive ball-like silver sulfide (acanthite) but with minor metallic silver and copper impurities. In FeS_2, the pyrite phase was dominating with marcasite residues at the particle boundaries characteristic of hydrothermal synthesis. For all materials, XPS spectra typical for air-exposed sulfides were recorded. In addition to the anticipated oxidation states of metals and sulfur, higher valences were also detected. In particular, a significant intrinsic contribution of Ni^{3+} was observed in nickel sulfide. The integration of optical studies and theoretical calculations indicated that CuS, Ag_2S, and FeS_2 are semiconductors with band gaps of 1.74, 0.98, and 1.14 eV, respectively, whereas α-NiS exhibits an intraband transition at 1.42 eV. Among the investigated TMSs, the highest sensitivity toward glucose showed nickel sulfide, but it was the least selective. Conversely, FeS_2 responded only to strong reductants. Finally, we established the correlation between the d-band center in the

TMS and its electrocatalytic activity. These findings may aid in selecting materials with optimized sensitivity and selectivity for non-enzymatic glucose sensors. Validating this approach on other groups of compounds would confirm its universality and advance sensor development.

CRediT authorship contribution statement

Anna Kusior: Writing – review & editing, Supervision, Methodology. **Marta Radecka:** Writing – review & editing, Supervision, Methodology. **Andrzej Mikuła:** Writing – original draft, Visualization, Validation, Methodology, Investigation, Formal analysis. **Julia Maria Mazurkow:** Writing – original draft, Visualization, Validation, Project administration, Methodology, Investigation, Funding acquisition, Formal analysis, Conceptualization.

Declaration of Competing Interest

The authors declare the following financial interests/personal relationships which may be considered as potential competing interests: Julia M. Mazurkow reports financial support was provided by National Science Centre Poland. If there are other authors, they declare that they have no known competing financial interests or personal relationships that could have appeared to influence the work reported in this paper.

Data availability

Data will be made available on request.

Acknowledgment

This research was funded by National Science Centre, Poland, grant no. 2021/41/N/ST8/03515. We would like to thank Andrzej Kałka and Mateusz Marzec for the scientific discussion.

Appendix A. Supporting information

Supplementary data associated with this article can be found in the online version at doi:10.1016/j.jallcom.2024.175749.

References

[1] International Diabetes Federation, IDF Diabetes Atlas, 10th edition, Brussels, 2021. ⟨www.diabetesatlas.org⟩.
[2] R. Wilson, A.P.F. Turner, Glucose oxidase: an ideal enzyme, Biosens. Bioelectron. 7 (1992) 165–185, https://doi.org/10.1016/0956-5663(92)87013-F.
[3] H. Lee, Y.J. Hong, S. Baik, T. Hyeon, D. Kim, Enzyme-based glucose sensor: from invasive to wearable device, Adv. Health Mater. 7 (2018) 1701150, https://doi.org/10.1002/adhm.201701150.
[4] S.P. Nichols, A. Koh, W.L. Storm, J.H. Shin, M.H. Schoenfisch, Biocompatible materials for continuous glucose monitoring devices, Chem. Rev. 113 (2013) 2528–2549, https://doi.org/10.1021/cr300387j.
[5] A. Yamaguchi, K. Arai, A.N.El Aisnada, J.E. Lee, N. Kitadai, R. Nakamura, M. Miyauchi, Multi-regression analysis of CO_2 electroreduction activities on metal sulfides, J. Phys. Chem. C. 126 (2022) 2772–2779, https://doi.org/10.1021/acs.jpcc.1c08993.
[6] W. Yang, X. Zhang, S.D. Tilley, Emerging binary chalcogenide light absorbers: material specific promises and challenges, Chem. Mater. 33 (2021) 3467–3489, https://doi.org/10.1021/acs.chemmater.1c00741.
[7] F. Jamal, A. Rafique, S. Moeen, J. Haider, W. Nabgan, A. Haider, M. Imran, G. Nazir, M. Alhassan, M. Ikram, Q. Khan, G. Ali, M. Khan, W. Ahmad, M. Maqbool, Review of metal sulfide nanostructures and their applications, ACS Appl. Nano Mater. 6 (2023) 7077–7106, https://doi.org/10.1021/acsanm.3c00417.
[8] K. Dhara, D.R. Mahapatra, Electrochemical nonenzymatic sensing of glucose using advanced nanomaterials, Microchim. Acta 185 (2018) 1–32, https://doi.org/10.1007/s00604-017-2609-1.
[9] T. Weber, R. Prins, R.A. Santen, eds., Transition Metal Sulphides, Springer Netherlands, Dordrecht, 1998. https://doi.org/10.1007/978-94-017-3577-3.
[10] K.E. Toghill, R.G. Compton, Electrochemical non-enzymatic glucose sensors: a perspective and an evaluation, Int J. Electrochem Sci. 5 (2010) 1246–1301, https://doi.org/10.1016/S1452-3981(23)15359-4.
[11] T.T. Aun, N.M. Salleh, U.F.Md Ali, N.S.A. Manan, Non-enzymatic glucose sensors involving copper: an electrochemical perspective, Crit. Rev. Anal. Chem. 53 (2023) 537–593, https://doi.org/10.1080/10408347.2021.1967720.
[12] G. Kaur, M. Kaur, A. Thakur, A. Kumar, Recent progress on pyrite FeS_2 nanomaterials for energy and environment applications: synthesis, properties and future prospects, J. Clust. Sci. 31 (2020) 899–937, https://doi.org/10.1007/s10876-019-01708-3.
[13] W.T. Hong, R.E. Welsch, Y. Shao-Horn, Descriptors of oxygen-evolution activity for oxides: a statistical evaluation, J. Phys. Chem. C. 120 (2016) 78–86, https://doi.org/10.1021/acs.jpcc.5b10071.
[14] N. Dubouis, A. Grimaud, The hydrogen evolution reaction: from material to interfacial descriptors, Chem. Sci. 10 (2019) 9165–9181, https://doi.org/10.1039/c9sc03831k.
[15] D. Pletcher, Electrocatalysis: present and future, J. Appl. Electrochem 14 (1984) 403–415, https://doi.org/10.1007/BF00610805.
[16] L.D. Burke, Premonolayer oxidation and its role in electrocatalysis, Electro Acta 39 (1994) 1841–1848, https://doi.org/10.1016/0013-4686(94)85173-5.
[17] J.M. Mazurków, A. Kusior, M. Radecka, Electrochemical characterization of modified glassy carbon electrodes for non-enzymatic glucose sensors, Sensors 21 (2021) 7928, https://doi.org/10.3390/s21237928.
[18] K. Momma, F. Izumi, *VESTA 3* for three-dimensional visualization of crystal, volumetric and morphology data, J. Appl. Crystallogr 44 (2011) 1272–1276, https://doi.org/10.1107/S0021889811038970.
[19] P. Blaha, K. Schwarz, F. Tran, R. Laskowski, G.K.H. Madsen, L.D. Marks, WIEN2k: an APW + lo program for calculating the properties of solids, J. Chem. Phys. 152 (2020) 074101, https://doi.org/10.1063/1.5143061.
[20] J.P. Perdew, A. Ruzsinszky, G.I. Csonka, O.A. Vydrov, G.E. Scuseria, L.A. Constantin, X. Zhou, K. Burke, Restoring the density-gradient expansion for exchange in solids and surfaces, Phys. Rev. Lett. 100 (2008) 136406, https://doi.org/10.1103/PhysRevLett.100.136406.
[21] A.D. Becke, E.R. Johnson, A simple effective potential for exchange, J. Chem. Phys. 124 (2006), https://doi.org/10.1063/1.2213970.
[22] J.M. Mazurków, A. Kusior, E. Partyka-Jankowska, M. Radecka, Unraveling the role of sodium thiosulfate in copper sulfide synthesis, Cryst. Growth Des. 24 (2024) 2475–2484, https://doi.org/10.1021/acs.cgd.3c01448.
[23] J.M. Mazurków, A. Kusior, A. Mikuła, M. Radecka, Transition metal sulfides for electrochemical applications: controlled chemical conversion of CuS to Ag_2S, Appl. Surf. Sci. 606 (2022) 154984, https://doi.org/10.1016/j.apsusc.2022.154984.
[24] I. Martina, R. Wiesinger, D. Jembrih-Simbuerger, M. Schreiner, Micro-Raman characterisation of silver corrosion products: instrumental set up and reference database, E-Preservation Sci. 9 (2012) 1–8.
[25] S.I. Sadovnikov, E.G. Vovkotrub, A.A. Rempel, Micro-Raman spectroscopy of nanostructured silver sulfide, Dokl. Phys. Chem. 480 (2018) 81–84, https://doi.org/10.1134/S0012501618060027.
[26] D.J. Vaughan, Sulfide mineralogy and geochemistry: introduction and overview, Rev. Miner. Geochem 61 (2006) 1–5, https://doi.org/10.2138/rmg.2006.61.1.
[27] D.A. Kitchaev, G. Ceder, Evaluating structure selection in the hydrothermal growth of FeS_2 pyrite and marcasite, Nat. Commun. 7 (2016) 13799, https://doi.org/10.1038/ncomms13799.
[28] F. Jiang, L.T. Peckler, A.J. Muscat, Phase pure pyrite FeS_2 nanocubes synthesized using oleylamine as ligand, solvent, and reductant, Cryst. Growth Des. 15 (2015) 3565–3572, https://doi.org/10.1021/acs.cgd.5b00751.
[29] B. Yuan, W. Luan, S. Tu, J. Wu, One-step synthesis of pure pyrite FeS_2 with different morphologies in water, N. J. Chem. 39 (2015) 3571–3577, https://doi.org/10.1039/C4NJ02243B.
[30] T.P. Mernagh, A.G. Trudu, A laser Raman microprobe study of some geologically important sulphide minerals, Chem. Geol. 103 (1993) 113–127, https://doi.org/10.1016/0009-2541(93)90295-T.
[31] O. Yousfi, P. Donnadieu, Y. Bréchet, F. Robaut, F. Charlot, A. Kasper, F. Serruys, Phase transformations in nickel sulphide: microstructures and mechanisms, Acta Mater. 58 (2010) 3367–3380, https://doi.org/10.1016/j.actamat.2010.02.011.
[32] M. Muniyappa, S.N. Kalegowda, M. Shetty, J.B. Sriramoju, M. Shastri, N.R. S.V., D, S.M.V. De, D. Rangappa, Cocatalyst free nickel sulphide nanostructure for enhanced photocatalytic hydrogen evolution, Int J. Hydrog. Energy 47 (2022) 5307–5318, https://doi.org/10.1016/j.ijhydene.2021.11.171.
[33] D.G. Moon, S. Rehan, S.Y. Lim, D. Nam, I. Seo, J. Gwak, H. Cheong, Y.S. Cho, Y. Lee, S. Ahn, Structural, optical and electrical impacts of marcasite in pyrite thin films, Sol. Energy 159 (2018) 930–939, https://doi.org/10.1016/j.solener.2017.11.026.
[34] M. Fantauzzi, B. Elsener, D. Atzei, A. Rigoldi, A. Rossi, Exploiting XPS for the identification of sulfides and polysulfides, RSC Adv. 5 (2015) 75953–75963, https://doi.org/10.1039/c5ra14915k.
[35] Yu.L. Mikhlin, G.L. Pashkov, E.V. Tomashevich, Defective nonstoichiometric layer on the real surface of sulfide minerals, J. Min. Sci. 29 (1993) 175–181, https://doi.org/10.1007/BF00733471.
[36] J.R. Mycroft, H.W. Nesbitt, A.R. Pratt, X-ray photoelectron and Auger electron spectroscopy of air-oxidized pyrrhotite: distribution of oxidized species with depth, Geochim Cosmochim. Acta 59 (1995) 721–733, https://doi.org/10.1016/0016-7037(94)00352-M.
[37] Y. Xie, A. Riedinger, M. Prato, A. Casu, A. Genovese, P. Guardia, S. Sottini, C. Sangregorio, K. Miszta, S. Ghosh, T. Pellegrino, L. Manna, Copper sulfide nanocrystals with tunable composition by reduction of covellite nanocrystals with Cu^+ ions, J. Am. Chem. Soc. 135 (2013) 17630–17637, https://doi.org/10.1021/ja409754v.
[38] S.W. Goh, A.N. Buckley, R.N. Lamb, Copper(II) sulfide, Min. Eng. 19 (2006) 204–208, https://doi.org/10.1016/j.mineng.2005.09.003.
[39] P. Kumar, R. Nagarajan, R. Sarangi, Quantitative X-ray absorption and emission spectroscopies: electronic structure elucidation of Cu_2S and CuS, J. Mater. Chem. C.

Mater. 1 (2013) 2448, https://doi.org/10.1039/c3tc00639e.
[40] J.R. Vegelius, K.O. Kvashnina, H. Hollmark, M. Klintenberg, Y.O. Kvashnin, I.L. Soroka, L. Werme, S.M. Butorin, X-ray spectroscopic study of Cu_2S, CuS, and copper films exposed to Na_2S solutions, J. Phys. Chem. C. 116 (2012) 22293–22300, https://doi.org/10.1021/jp302390c.
[41] A. Morales-García, A.L. Soares, E.C. Dos Santos, H.A. De Abreu, H.A. Duarte, First-principles calculations and electron density topological analysis of covellite (CuS), J. Phys. Chem. A 118 (2014) 5823–5831, https://doi.org/10.1021/jp4114706.
[42] I.I. Mazin, Structural and electronic properties of the two-dimensional superconductor CuS with 1 -valent copper, Phys. Rev. B 85 (2012) 115133, https://doi.org/10.1103/PhysRevB.85.115133.
[43] S.W. Goh, A.N. Buckley, R.N. Lamb, R.A. Rosenberg, D. Moran, The oxidation states of copper and iron in mineral sulfides, and the oxides formed on initial exposure of chalcopyrite and bornite to air, Geochim Cosmochim. Acta 70 (2006) 2210–2228, https://doi.org/10.1016/j.gca.2006.02.007.
[44] A.M. Ferraria, A.P. Carapeto, A.M. Botelho Do Rego, X-ray photoelectron spectroscopy: Silver salts revisited, Vacuum 86 (2012) 1988–1991, https://doi.org/10.1016/j.vacuum.2012.05.031.
[45] W. Yu, J. Yin, Y. Li, B. Lai, T. Jiang, Y. Li, H. Liu, J. Liu, C. Zhao, S.C. Singh, J. Chen, B. Lin, H. Idriss, C. Guo, Ag_2S quantum dots as an infrared excited photocatalyst for hydrogen production, ACS Appl. Energy Mater. 2 (2019) 2751–2759, https://doi.org/10.1021/acsaem.9b00091.
[46] B. Balakrishnan, S.K. Balasingam, K. Sivalingam Nallathambi, A. Ramadoss, M. Kundu, J.S. Bak, I.H. Cho, P. Kandasamy, Y. Jun, H.-J. Kim, Facile synthesis of pristine FeS_2 microflowers and hybrid rGO-FeS_2 microsphere electrode materials for high performance symmetric capacitors, J. Ind. Eng. Chem. 71 (2019) 191–200, https://doi.org/10.1016/j.jiec.2018.11.022.
[47] M.V. Morales-Gallardo, A.M. Ayala, M. Pal, M.A. Cortes Jacome, J.A. Toledo Antonio, N.R. Mathews, Synthesis of pyrite FeS_2 nanorods by simple hydrothermal method and its photocatalytic activity, Chem. Phys. Lett. 660 (2016) 93–98, https://doi.org/10.1016/j.cplett.2016.07.046.
[48] H.W. Nesbitt, I.J. Muir, X-ray photoelectron spectroscopic study of a pristine pyrite surface reacted with water vapour and air, Geochim Cosmochim. Acta 58 (1994) 4667–4679, https://doi.org/10.1016/0016-7037(94)90199-6.
[49] Y. Ouyang, Y. Chen, J. Peng, J. Yang, C. Wu, B. Chang, X. Guo, G. Chen, Z. Luo, X. Wang, Nickel sulfide/activated carbon nanotubes nanocomposites as advanced electrode of high-performance aqueous asymmetric supercapacitors, J. Alloy. Compd. 885 (2021) 160979, https://doi.org/10.1016/j.jallcom.2021.160979.
[50] J. Wu, S. Liu, Y. Rehman, T. Huang, J. Zhao, Q. Gu, J. Mao, Z. Guo, Phase engineering of nickel sulfides to boost sodium- and potassium-ion storage performance, Adv. Funct. Mater. 31 (2021) 2010832, https://doi.org/10.1002/adfm.202010832.
[51] B. Guan, Y. Li, B. Yin, K. Liu, D. Wang, H. Zhang, C. Cheng, Synthesis of hierarchical NiS microflowers for high performance asymmetric supercapacitor, Chem. Eng. J. 308 (2017) 1165–1173, https://doi.org/10.1016/j.cej.2016.10.016.
[52] G.Y. Shaikh, D.S. Nilegave, S.S. Girawale, K.B. Kore, S.R. Newaskar, S.A. Sahu, A.M. Funde, Structural, optical, photoelectrochemical, and electronic properties of the photocathode CuS and the efficient CuS/CdS heterojunction, ACS Omega 7 (2022) 30233–30240, https://doi.org/10.1021/acsomega.2c03352.
[53] I.J. Ferrer, D.M. Nevskaia, C. de las Heras, C. Sánchez, About the band gap nature of FeS_2 as determined from optical and photoelectrochemical measurements, Solid State Commun. 74 (1990) 913–916, https://doi.org/10.1016/0038-1098(90)90455-K.
[54] D.M. Roessler, Kramers-Kronig analysis of reflection data, Br. J. Appl. Phys. 16 (1965) 1119–1123, https://doi.org/10.1088/0508-3443/16/8/310.
[55] Y. Bi, Y. Yuan, C.L. Exstrom, S.A. Darveau, J. Huang, Air stable, photosensitive, phase pure iron pyrite nanocrystal thin films for photovoltaic application, Nano Lett. 11 (2011) 4953–4957, https://doi.org/10.1021/nl202902z.
[56] S.D. Sartale, C.D. Lokhande, Preparation and characterization of nickel sulphide thin films using successive ionic layer adsorption and reaction (SILAR) method, Mater. Chem. Phys. 72 (2001) 101–104, https://doi.org/10.1016/S0254-0584(01)00314-5.
[57] P.C. Patel, P.K. Mishra, J. Kashyap, S. Awasthi, Cation doped approach for photodegradation of 4-chlorophenol by highly efficient solar active NiS photocatalyst: The case of Cu^{2+} doping, J. Photochem. Photobio. A Chem. 437 (2023) 114499, https://doi.org/10.1016/j.jphotochem.2022.114499.
[58] M. Fleischmann, K. Korinek, D. Pletcher, The kinetics and mechanism of the oxidation of amines and alcohols at oxide-covered nickel, silver, copper, and cobalt electrodes, J. Chem. Soc., Perkin Trans. 2 47 (1972) 1396, https://doi.org/10.1039/p29720001396.
[59] P. Luo, F. Zhang, R.P. Baldwin, Comparison of metallic electrodes for constant-potential amperometric detection of carbohydrates, amino acids and related compounds in flow systems, Anal. Chim. Acta 244 (1991) 169–178, https://doi.org/10.1016/S0003-2670(00)82494-0.
[60] F. Franceschini, I. Taurino, Nickel-based catalysts for non-enzymatic electrochemical sensing of glucose: a review, Phys. Med. 14 (2022) 100054, https://doi.org/10.1016/j.phmed.2022.100054.
[61] J. Deng, Z.-Y. Zhao, Effects of non-stoichiometry on electronic structure of Cu_xS_y compounds studied by first-principle calculations, Mater. Res Express 6 (2019) 105513, https://doi.org/10.1088/2053-1591/ab3874.
[62] M.-Y. Zhang, H. Jiang, Accurate prediction of band structure of FeS2: a hard quest of advanced first-principles approaches, Front Chem. 9 (2021) 747972, https://doi.org/10.3389/fchem.2021.747972.
[63] D.W. Bullett, Electronic structure of 3d pyrite- and marcasite-type sulphides, J. Phys. C: Solid State Phys. 15 (1982) 6163–6174, https://doi.org/10.1088/0022-3719/15/30/010.
[64] Y. Tang, H. Yang, J. Sun, M. Xia, W. Guo, L. Yu, J. Yan, J. Zheng, L. Chang, F. Gao, Phase-pure pentlandite $Ni_{4.3}Co_{4.7}S_8$ binary sulfide as an efficient bifunctional electrocatalyst for oxygen evolution and hydrogen evolution, Nanoscale 10 (2018) 10459–10466, https://doi.org/10.1039/C8NR02402B.
[65] D.D. Sarma, S.R. Krishnakumar, N. Chandrasekharan, E. Weschke, C. Schüßler-Langeheine, L. Kilian, G. Kaindl, Electronic Structure of $NiS_{1-x}Se_x$ across the Phase Transition, Phys. Rev. Lett. 80 (1998) 1284–1287, https://doi.org/10.1103/PhysRevLett.80.1284.
[66] K.C. Leonard, A.J. Bard, Pattern recognition correlating materials properties of the elements to their kinetics for the hydrogen evolution reaction, J. Am. Chem. Soc. 135 (2013) 15885–15889, https://doi.org/10.1021/ja407394q.
[67] L. Wu, J.P. Hofmann, High-entropy transition metal chalcogenides as electrocatalysts for renewable energy conversion, Curr. Opin. Electrochem 34 (2022) 101010, https://doi.org/10.1016/j.coelec.2022.101010.
[68] B. Zhao, X. Long, Q. Zhao, M. Shakouri, R. Feng, L. Lin, Y. Zeng, Y. Zhang, X.-Z. Fu, J.-L. Luo, In situ self-heterogenization of Cu_2S/CuS nanostructures with modulated d band centers for promoting photocatalytic degradation and hydrogen evolution performances, Mater. Today Nano 23 (2023) 100362, https://doi.org/10.1016/j.mtnano.2023.100362.
[69] H. Ooka, J. Huang, K.S. Exner, The sabatier principle in electrocatalysis: basics, limitations, and extensions, Front Energy Res 9 (2021) 654460, https://doi.org/10.3389/fenrg.2021.654460.